Energy Conversion and Management 75 (2013) 162–174

Contents lists available at SciVerse ScienceDirect

Energy Conversion and Management

journal homepage: www.elsevier.com/locate/enconman

Electrochemical–thermal analysis of 18650 Lithium Iron Phosphate cell

L.H. Saw, Yonghuang Ye, A.A.O. Tay *

Department of Mechanical Engineering, Faculty of Engineering, National University of Singapore, 117576 Singapore, Singapore

ARTICLE INFO

Article history:
Received 13 December 2012
Accepted 24 May 2013

Keywords:
Battery temperature
Electrochemical
Heat generation
Lithium ion battery

ABSTRACT

A pseudo two dimensional electrochemical coupled with lumped thermal model has been developed to analyze the electrochemical and thermal behavior of the commercial 18650 Lithium Iron Phosphate battery. The cell was cut to obtain the physical dimension of the current collector, electrodes, separator, casing thickness, gasket, etc. The layer structure of the spiral wound, cylindrical casing, gasket and heat shrink wrapping were modeled to understand better the temperature distribution across the cell. Natural convection and radiation were used to reflect the heat dissipation on the side surface. Experimental study was carried out to validate the simulation results. The simulation results suggested that the cell temperature and total heat generation rate have a positive correlation with the I_t-rates and these were inline with the experimental results. Reaction heat was the main heat source and it contributed about 80–85% of the total heat generated during charging and discharging of the cell. Based on the simulation results, the final temperature of the cell surface was elevated to 59 °C using $10I_t$ of charging. The effect of electrical contact resistance between the connectors and terminals of the cell was also investigated. It was found that the electrical contact resistance caused a large temperature gradient across the cell. These effects are important and should be considered in the design of EV battery pack and thermal management system to reduce the maximum temperature and maintain the temperature uniformity of the cells.

1. Introduction

Depleting fuels source and increasing environmental awareness are some of the main challenges in the automotive industry. Electric Vehicles (EVs) and Hybrid Electric Vehicles (HEVs) are projected as one of the most sustainable solutions for future transport. However, the performance and thermal management of the battery pack with respect to the life cycle and related warranty cost are some of the significant challenges faced by automakers. The Lithium ion (Li-ion) battery which boasts of high power and energy density was used to replace Nickel Metal Hydride (NiMH) and lead acid batteries which have lower energy density and depth of discharge (DOD) in EVs and HEVs [1–4]. Various chemistries of the Li-ion battery are being studied. For example, different types of cathode material ($LiCoO_2$, $LiMn_2O_4$, $LiFePO_4$ and $LiVPO_4$), anode material (graphite, hard carbon, $Li_4Ti_5O_{12}$, $Li_{4.4}Si$ and $Li_{4.4}Ge$) and electrolyte ($LiPF_6$, $LiBF_4$ and $LiClO_4$) have been synthesized to produce different structural configurations of the battery such as spiral wound, elliptic and stacked plate [4–6]. At high charging/discharging rates, electrochemical reactions occur at faster rates and the cells are prone to extensive heat generation. Localized heat accumulation will lead to excessive temperature rise that can initiate electrolyte ignition resulting in thermal runaway and in the worst case-explosion. Therefore, the study on the thermal behavior of the Li-ion battery is necessary to ensure the safety and optimum electrochemical process in the battery.

Several researchers have developed the mathematical models to predict the electrochemical process occurring within the Li-ion battery, charging and discharging behavior and various thermal models have been established to explain the heat generated in the battery [7–20]. Most of the studies are focused on the $LiCoO_2$ [10–13] or $LiMn_2O_4$ [14–18] system using electrochemical–thermal models. The thermal models employed in these studies range from lumped models-treating the layer structure of the cells as homogeneous material with effective thermal properties, assuming a uniform cell temperature distribution, heat generation data obtained from experiments to detailed models that couple the electrochemical model with the thermal model using heat generation and temperature dependent physical properties. Most of these thermal models did not consider the outer can and the heat shrink wrapping present in commercially available batteries and the influence of contact resistance between the battery terminals and the external connectors. The dimensionality of the models range from one to three-dimensions depending on the complexity of the physical phenomenon considered. Most of the three-dimensional models do not consider the electrochemical phenomena and are purely thermal models based on the lumped capacity approach [19–25].

* Corresponding author. Tel.: +65 65162207; fax: +65 67791459.
E-mail address: mpetayao@nus.edu.sg (A.A.O. Tay).

0196-8904/$ - see front matter © 2013 Elsevier Ltd. All rights reserved.
http://dx.doi.org/10.1016/j.enconman.2013.05.040

Nomenclature

a	specific interfacial area of the electrode, m^{-1}
c	lithium concentration at the electrode/electrolyte interface, mol m^{-3}
A_{cc}	electrical connector contact area on the terminal, m^2
C_{dl}	electrical double layer capacitance, F m^{-2}
C_p	specific heat capacity for the active battery material, J kg^{-1} K^{-1}
C_{bp}	theoretical capacity of the battery, Ah
D	diffusion coefficient of Li-ion, m^2 s^{-1}
E	emissivity
E_{eq}	open circuit voltage, OCV, V
$E_{0,ref}$	equilibrium potential at reference temperature, V
$\frac{\partial E_{eq}}{\partial T}$	temperature derivative of equilibrium potential, V K^{-1}
F	Faraday's constant, C mol^{-1}
f	mean molar activity coefficient of the electrolyte
h	convective heat transfer coefficient, W m^{-2} K^{-1}
I^k_{dis}	discharge current, A
i	current density vector in a phase, A m^{-2}
i_{ioc}	transfer current density of a reaction at the electrode/electrolyte interface, A m^{-2}
i_0	exchange current density of an electrode reaction, A m^{-2}
j	transfer current resulted from the intercalation or de-intercalation of Li, A m^{-3}
k	electrochemical reaction rate constant, m s^{-1}
k_T	effective thermal conductivity of the active battery material, W m^{-1} K^{-1}
L	thickness of the different layers of the cell, m
R	universal gas constant, J mol^{-1} K^{-1}
R_{SEI}	solid/electrolyte interfacial film resistance, Ω m^2
R_{cc}	contact resistance, Ω m^2
r_s	radius of the spherical particle, m
T	absolute temperature, K
T_∞	free stream temperature, K
T_{dis}	discharge time, h
t_+	transport number
Vol	volume of the cylindrical cell, m^3
z	$\frac{c_s}{c_{max}}$
α	charge transfer coefficients
σ	electric conductivity, S m^{-1}
ε	volume fraction of a phase
η	activation over-potentials of an electrode reaction, V
ξ	porosity of the specimen
ϕ_s	electric potential, V
ϕ_l	electrolyte potential, V
ρ	effective density of the active battery material, kg m^{-3}
σ_{sb}	Stefan-Boltzmann constant, W m^{-2} K^{-4}

Subscripts

a	negative electrode
c	positive electrode
ang	angular direction
eff	effective
f	filler volume fraction
i	different layer of active battery material
l	electrolyte phase
max	maximum
r	radial direction
ref	reference state
s	solid phase
SEI	solid electrolyte interface
0	initial value

$LiFePO_4$ (LFP) electrode with olivine structure is a promising candidate electrode material for electric vehicle battery. The LFP batteries have high thermal stability, nontoxic and less expensive as compared to other cathode materials such as $LiCoO_2$, $LiMn_2O_4$, $LiNiO_2$, etc. Besides, LFP also differs from other cathode materials with a phase change associated with various stage of lithiation and do not release oxygen at elevated temperatures which will cause thermal runaway of the cell [4,5,26]. Very few modeling works have been carried out to investigate the behavior of LFP [5,21,27].

Apart from studies on a single cell, energy management studies are conducted on battery packs as well. Minimization of the energy loss in the cells assemblies to allow maximization of the energy harvesting in the battery pack is very crucial in the energy management. The effect of the electrical contact resistance at the contact interface of the cell terminal and the bus bar has been overlooked. High electrical contact resistance will cause difficulty in the cell balancing, large variation of the cell temperature, reduce the storage capability of the cell and lead to localized heating and in the extreme case lead to cell explosion. A recent study established that the electrical contact resistance due to imperfect surface features between the connectors and cell terminal will cost about 20% loss in the total energy flow in and out of the battery [28]. Panasonic has changed the design of the NiMH module current collector to reduce the hot spots and improved the cell performance [29]. However, the current studies is based on electro-thermal model with single internal resistance value of the cell and neglect the transient behavior of the electrochemical changes in the battery during the charging and discharging [29].

In view of the above, the aim of this work is twofold: First, to investigate the electrochemical and thermal behavior of a commercially available 18650 LFP battery using mathematical modeling and experiments and seconds to apply the developed model to study the effect of contact resistance between the cell terminals and external connectors. A pseudo two-dimensional electrochemical model is coupled with a lumped three-dimensional thermal model to predict the electrochemical and thermal behavior of spirally wound LFP battery. The model predictions are compared with experimental data. The models are useful to provide fundamental understanding of the internal transport of the Li-ion and theoretical reference for the battery cooling system design for fast charging battery in EVs or HEVs applications.

2. Mathematical model

2.1. Pseudo two-dimensional electrochemical model

A schematic diagram of the 18650 LFP cell electrochemical model is shown in Fig. 1. The cell was cut to obtain the physical dimension of the current collector, electrodes, separator, casing thickness, gasket, etc as shown in Fig. 2. The thickness of the current collectors, electrodes, separator, outer can and heat shrink wrap are measured using LEICA DM 2500 M optical microscope. The height and length of the electrodes are measured with the stainless steel ruler. The dimensions and parameters used in modeling are tabulated in Tables 1 and 2. During the charging process, the lithium ions intercalate into solid particles of the negative electrode and de-intercalate from solid particles of the positive

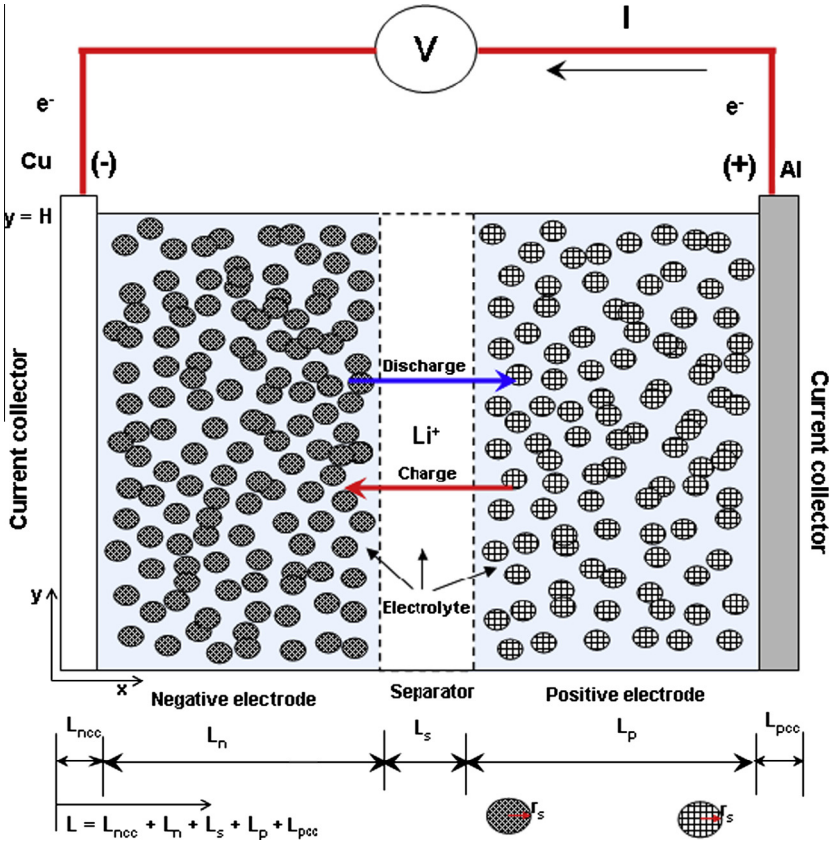

Fig. 1. Schematic of 18650 LFP cell electrochemical model.

electrode. The electrons released during the process will flow through the external circuit to the negative electrode. This traveling direction will be reversed during the discharging process. Heat is generated within the cell and dissipated to all directions. The electrochemical reactions are represented by Eqs. (1) and (2).

Positive electrode

$$LiC_6 \underset{\text{discharge}}{\overset{\text{charge}}{\leftrightarrows}} Li_{1-x}C_6 + xLi^+ + e^- \tag{1}$$

Negative electrode

$$xLi + xe^- + Li_{1-x}FePO_4 \underset{\text{discharge}}{\overset{\text{charge}}{\leftrightarrows}} LiFePO_4 \tag{2}$$

Porous electrode theory is used to model the electrode which consists of active materials and electrolyte. The solid active material and electrolyte are treated as superimposed with own volume fraction of ε_s and ε_l respectively. Electrolyte diffusion ($D_{l,eff} = \varepsilon_l^{3/2} D_l$), conductivity ($\sigma_{l,eff} = \varepsilon_l^{3/2}\sigma_l$) and electrical conductivity in the electrode $\sigma_{s,eff} = (1 - \varepsilon_l - \varepsilon_f)^{3/2}\sigma_s$ are corrected with Bruggeman factor to account for the porosity and tortuosity effect [9,16]. The current density (is) and charge balance based on the Ohm's law in the electrode are defined in Eqs. (3) and (4) respectively [9,16].

$$i_s = \sigma_{s,eff}\nabla\phi_s \tag{3}$$

$$\nabla \cdot i_s = j \tag{4}$$

The transfer current (j) resulted from Li insertion and removal is expressed as in Eq. (5) [18].

$$j = \begin{cases} a_{s,a} i_{loc,a} & \text{in the negative electrode} \\ 0 & \text{in the separator} \\ a_{s,c} i_{loc,c} & \text{in the positive electrode} \end{cases} \tag{5}$$

Reaction rates for intercalation and de-intercalation reaction of Li as in Eqs. (1) and (2) are assumed to follow the Butler–Volmer rule as shown in Eq. (6) [9,25].

$$i_{loc} = i_0 \left\{ \exp\left[\frac{\alpha_a F}{RT}(\eta)\right] - \exp\left[-\frac{\alpha_c F}{RT}(\eta)\right] \right\} \tag{6}$$

The exchange current density (i_0) depends on the lithium concentrations in the electrolyte and solid active materials as in Eq. (7) [25]. k_c and k_a is determined by initial species concentration and exchange current density.

$$i_0 = F(k_c)^{\alpha_a}(k_a)^{\alpha_c}(c_{s,max} - c_s)^{\alpha_a}(c_s)^{\alpha_c}\left(\frac{c_l}{c_{l,ref}}\right)^{\alpha_a} \tag{7}$$

A resistive film which is also known as Solid Electrolyte Interface (SEI) is form on the solid particles. The SEI causes additional loss on the electrodes. To model the SEI, an extra solution variable for the potential variation over the film is incorporated. The governing equation is defined as in Eq. (8) [18].

$$\Delta\phi_{s,SEI} = i_{loc} R_{SEI} \tag{8}$$

Due to the lack of clear physical justification of RSEI, zero value of RSEI is used in the present work. The activation over-potential for all electrode reactions in the electrode then received an extra potential contribution and defined as in Eq. (9) [18].

$$\eta = \phi_s - \Delta\phi_{s,SEI} - \phi_l - E_{eq} \tag{9}$$

The equilibrium potential is a function of State of Charge (SOC) and temperature. It can be approximated by Taylor's first expansion as shown in Eq. (10) [16].

$$E_{eq} = E_{0,ref} + (T - T_{ref})\frac{\partial E_{eq}}{\partial T} \tag{10}$$

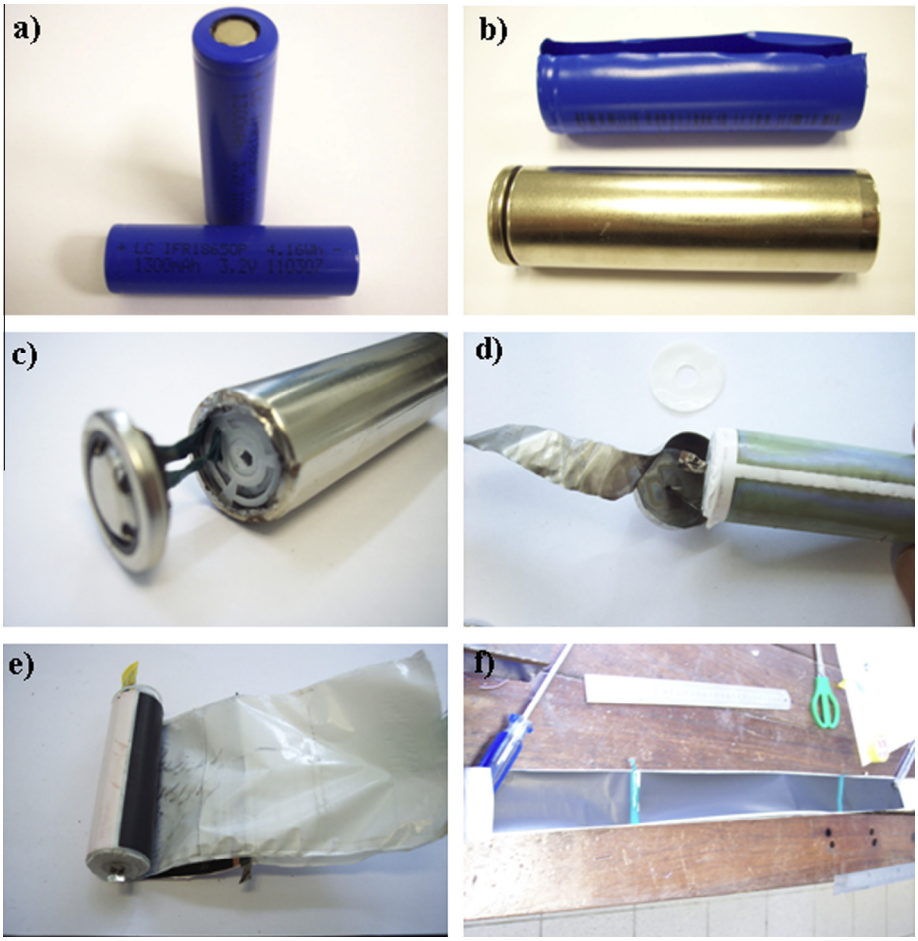

Fig. 2. (a) 18650 cell, (b) after stripping off the heat shrink wrapping, (c) positive terminal, (d) negative terminal, (e) unroll the spiral wound, and (f) tab and coated electrode material on the current material.

Table 1
Thermal and electrical cell specifications of the investigated LFP cell.

Parameter	Value	Parameter	Value
Nominal voltage, V	3.2	Cu current collector thickness, μ m	20
Nominal capacity, Ah	1.3	Al current collector thickness, μ m	10
Cell weight, g	30	Separator thickness, μ m	10
Can thickness, mm	0.3	Positive electrode height, cm	5.65
Heat shrink wrap material	PVC	Negative electrode height, cm	5.8
Heat shrink wrap thickness, μm	15	Positive electrode length, cm	7.6
Mandrel diameter, mm	4.0	Negative electrode length, cm	8.3
Positive electrode mass, g	14.88	Negative electrode mass, g	11.83
Positive electrode thermal conductivity, W m^{-1} K^{-1}	0.20	Positive electrode thickness (2sided), μ m	130
Negative electrode thermal conductivity, W m^{-1} K^{-1} [30]	1.04	Negative electrode thickness (2sided), μ m	90
Positive current collector thermal conductivity, W m^{-1} K^{-1} [30]	170	Heat capacity positive electrode, J kg^{-1} K^{-1} [31]	750
Negative current collector thermal conductivity, W m^{-1} K^{-1} [30]	398	Heat capacity negative electrode, J kg^{-1} K^{-1} [30]	1437
Positive current collector density, kg m^{-3} [30]	2770	Heat capacity positive current collector, J kg^{-1} K^{-1} [30]	875
Negative current collector density, kg m^{-3} [30]	8933	Heat capacity negative current collector, J kg^{-1} K^{-1} [30]	385
Positive electrode density, kg m^{-3} [32]	3600	Separator heat capacity, J kg^{-1} K^{-1} [30]	1978
Negative electrode density, kg m^{-3} [30]	1347	Separator density, kg m^{-3} [30]	1009
Separator thermal conductivity, W m^{-1} K^{-1} [30]	0.3344	Electrolyte thermal conductivity, W m^{-1} K^{-1} [30]	0.6
Electrolyte density, kg m^{-3} [30]	1130	Electrolyte heat capacity, J kg^{-1} K^{-1} [30]	2055

In the current study, the open circuit voltage for LFP [27] and graphite [39] electrodes at 25 °C are represented by Eqs. (11) and (12) respectively.

$$E_{eq,c} = 2.567462 + 57.69[1 - \tanh(100z + 2.9163927)] + 0.442953\tan^{-1}(-65.41928z + 64.89741) + 0.097237\tan^{-1}(-160.9058z + 154.590) \quad (11)$$

Table 2
Model input parameters for simulation of 1.3 Ah cell.

Parameter	Negative electrode	Separator	Positive electrode
Particle radius, r (m) [18,33]	12.5×10^{-6}	N/A	1.0×10^{-6}
Filler volume fraction, ε_f [18]	0.172	0.276	0.259
Electrolyte phase volume fraction, ε_l [18]	0.357	0.724	0.444
Maximum Li concentration in solid, $c_{s,max}$ (mol m^{-3}) [34]	26390	N/A	22800
Electric conductivity, σ (S m^{-1}) [35–36]	100	N/A	0.04
Initial electrolyte concentration, $c_{s,0}$ (mol m^{-3}) [18]	2000	2000	2000
Charge transfer coefficient, α_a, α_c [33]	0.5, 0.5	N/A	0.5, 0.5
SEI film resistance, R_{SEI} (Ω m^2)	0	N/A	0
Electrolyte mean molar activity coefficient, f [33]	1.0	1.0	1.0
Li diffusion coefficient in solid, D (m^2 s^{-1}) [18,32]	3.9×10^{-14}	N/A	8×10^{-14}
Li diffusion coefficient in electrolyte, D (m^2 s^{-1}) [27]	3×10^{-10}	3×10^{-10}	3×10^{-10}
Bruggeman tortuosity exponent [35]	1.5	1.5	1.5
Charge-transfer coefficients, α_a, α_c [34]	0.5	N/A	0.5
$1I_t$ discharge/charging current density, I (A m^{-2})	0	N/A	10
Electrical double layer capacitance, C_{dl} (F m^{-2}) [27]	0.2	N/A	0.08
Transport number of Li-ion, t_+ [25]	0.22		
Reference temperature, T_{ref} (K)	298.15		
Stefan-Boltzmann constant, σ (W m^{-2} K^4)	5.67×10^{-8}		
Emissivity of heat shrink wrapping, ε [37]	0.95		
Emissivity of battery casing [37]	0.19		
Connector contact resistance, R_{cc} (Ω) [38]	0.01		
Faraday's constant, F (C mol^{-1})	96487		
Universal gas constant, R (J mol^{-1} K^{-1})	8.3145		
Heat Transfer coefficient, W m^{-2} K^{-1} (estimated)	5		

$$\begin{aligned} E_{eq,a} =& 0.6379 + 0.5416\exp(-305.5309z) \\ &+ 0.044\tanh[-(z-0.1958)/0.1088] \\ &- 0.1978\tanh[(z-1.0571)/0.0854] \\ &- 0.6875\tanh[(z+0.0117)/0.0529] \\ &- 0.0175 tanh[(z-0.5692)/0.0875] \end{aligned} \quad (12)$$

The dE_{eq}/dT of carbon [40] and LiFePO4 [41] electrodes in function equilibrium potential vs. SOC correlations are shown in Fig. 3.

Conservation of charge during the electrolyte phase is also governed by Ohm law as below [25].

$$\nabla \cdot \left(\sigma_{l,eff} \nabla \phi_l + \frac{2\sigma_{l,eff} RT}{F} \left(1 + \frac{\partial \ln f}{\partial \ln c_l} \right) (t_+ - 1) \nabla \ln c_l \right) = -j \quad (13)$$

Concentrated solution theory is used to model the transport process in the electrolyte phase. The electrolyte is treated as a binary with single organic solvent [9,25]. The conservation of Li-ion in the electrolyte can be defined as below [18].

$$\frac{\partial(\varepsilon_l c_l)}{\partial t} = \nabla \cdot (D_{l,eff} \nabla c_l) + \frac{1 - t_+}{F} j \quad (14)$$

Concentration dependent function is used to model the conductivity of the electrolyte consisting of $LiPF_6$ in 1:1 mixture of Ethylene Carbonate (EC) and Diethylene Carbonate (DEC). The resulting electrolyte conductivity used in the model is defined in Eq. (15) [36].

$$\sigma_l = \sigma_{ref} \left(\frac{1.262(c/c_{ref})}{1 + 0.2(c/c_{ref})^2 + 0.08(c/c_{ref})^4} + 0.014 \right) \quad (15)$$

$$\sigma_{ref} = 7.8 \text{ m S cm}^{-1}, c_{ref} = 1 \text{ mol dm}^{-3}$$

The electrode is assumed to consist of spherical particles with the reaction occurring on the particle surface and the Lithium diffuses to and from the surface of the particles. The mass balance of Li-ion in the particles is governed by Fick's second law in the spherical coordinates as in Eq. (16) [25].

$$\frac{\partial c_s}{\partial t} = \nabla \cdot (D_s \nabla c_s) \quad (16)$$

The specific surface area of an electrode composed of the particle with spherical morphology is defined as in Eq. (17) [18]. In this model, the particle size is assumed to be uniformly distributed.

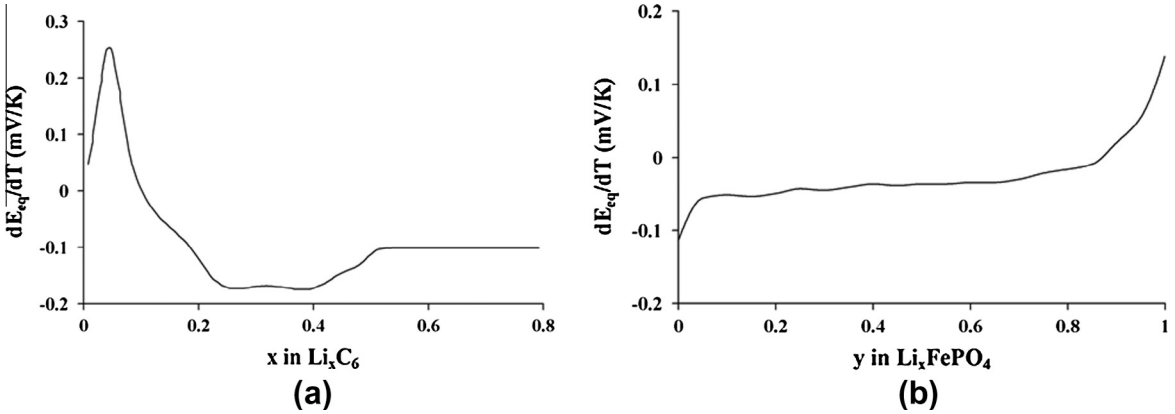

Fig. 3. Entropic heats as a function of SOC for: (a) carbon and (b) $LiFePO_4$.

$$a_s = \frac{3}{r_s}(1-\varepsilon_l-\varepsilon_f) \tag{17}$$

The electrochemical double layer capacitance is a dynamic phenomenon associated with the activation phenomenon which is related to the electric charge population. During the charging/discharging process, electrons will accumulate on the electrode side while Li-ion will accumulate on the electrolyte side. Helmholtz layer which is equal to an electric capacitor will be created and two different conductive areas are in contact [42]. The effect of double layer capacitance is also considered and modeled using Eq. (18) [43].

$$i_{dl} = \left(\frac{\partial \phi_s}{\partial t} - \frac{\partial \phi_l}{\partial t}\right) a_s C_{dl} \tag{18}$$

The electrolyte is assumed to be confined within the cell and there is no reaction on surfaces of the anode and cathode current collector. The boundary conditions for electrolyte are defined as below [18]:

$$-D_{l,eff}\frac{\partial c_l}{\partial x}\bigg|_{x=L_{ncc}} = -D_{l,eff}\frac{\partial c_l}{\partial x}\bigg|_{x=L_{ncc}+L_n+L_s+L_p} = 0 \tag{19}$$

$$-\sigma_{l,eff}\frac{\partial \phi_l}{\partial x}\bigg|_{x=L_{ncc}} = -\sigma_{l,eff}\frac{\partial \phi_l}{\partial x}\bigg|_{x=L_{ncc}+L_n+L_s+L_p} = 0 \tag{20}$$

In the separator, the entire current is carried by the lithium ions and therefore there is continuity of charge and species flux in the liquid phase across the electrode/separator interface. The charge flux will be equal to the total current density.

Insulating conditions apply for the solid phase current in the electrode/separator interface. The condition is provided below in Eq. (21) [18].

$$-\sigma_{s,eff}\frac{\partial \phi_s}{\partial x}\bigg|_{x=L_{ncc}+L_n} = -\sigma_{s,eff}\frac{\partial \phi_s}{\partial x}\bigg|_{x=L_{ncc}+L_n+L_s} = 0 \tag{21}$$

The charge flux at current collector is equal to the current density applied to the cell. The boundary conditions are defined as in Eq. (22) [18].

$$-\sigma_{s,eff}\frac{\partial \phi_s}{\partial x}\bigg|_{x=L_{ncc}+L_n+L_s+L_p+L_{pcc}} = \frac{I}{A} \tag{22}$$

The solid phase potential is set to be zero in the negative current collector boundary or in other words, the negative current collector is grounded [18].

$$\phi_s|_{x=0} = 0 \tag{23}$$

At the center of the spherical particle of the active material there is no flux. The boundary conditions are defined as below [18].

$$\frac{\partial c_s}{\partial r}\bigg|_{r=0} = 0 \qquad -D_s\frac{\partial c_s}{\partial r}\bigg|_{r=r_s} = \frac{j}{a_s F} \tag{24}$$

2.2. Lumped thermal model

A schematic diagram of the 18650 LFP cell thermal model is shown in Fig. 4. The resistance to conduction within the solid is much less than the resistance to convection outside the battery surface. Therefore, it can be assumed that the temperature profile in the cell is fairly uniform [44]. The chemistry of the cell is not affected significantly by small variation of temperature. Therefore, the electrochemical model is coupled to lumped thermal model to determine the temperature distribution of the entire cell. It is assumed that the temperature effect on the battery chemistry is negligible. The general thermal energy equation used to model the heat conduction for the cell is defined in Eq. (25) [35].

$$\rho_{eff}C_{p,eff}\frac{dT}{dt} = \nabla\cdot k_T\nabla T + Q_r + Q_j + Q_{rev} + Q_c \tag{25}$$

The boundary conditions of the Li-ion battery are determined by Newton's cooling law and thermal radiation [16]:

$$-k_{T,eff}\frac{\partial T}{\partial x}\bigg|_{x=L} = h(T-T_\infty) + E\sigma_{sb}(T^4 - T_\infty^4) \tag{26}$$

The total reaction heat generation rate is defined as below [16]:

$$Q_r = i_{loc}a_s(\phi_s - \phi_l - E_{eq}) \tag{27}$$

The total ohmic heat generation rate is defined as below [16]:

$$Q_j = \sigma_{s,eff}\nabla\phi_s\cdot\nabla\phi_s + \left(\sigma_{l,eff}\nabla\phi_l\cdot\nabla\phi_l + \frac{2\sigma_{l,eff}RT}{F}(t_+-1)\left(1+\frac{\partial \ln f}{\partial \ln c_l}\right)\nabla\ln c_l\cdot\nabla\phi_l\right) \tag{28}$$

The total reversible heat generation rate is defined as below [16]:

$$Q_{rev} = i_{loc}a_s T\left(\frac{\partial E_{eq}}{\partial T}\right) \tag{29}$$

The heat generation rate due to effect of connector contact resistance (R_{cc}) is neglected in the 1st part of the study is defined as below [35]:

$$Q_c = \left(I^2\frac{R_{cc}}{A_{cc}}\right)\Big/ Vol \tag{30}$$

The battery consists of several layers of electrodes and separator wound spirally into a cylinder. Therefore, the thermal conductivity in the battery model is considered anisotropic. The thermal conductivity is higher in axial direction compared to radial direction for the current geometry of 18650 LFP cell [30]. Hence, the thermal conductivity in radial and axial direction is defined as follow [30]:

$$k_{T,r} = \frac{\sum L_i}{\sum L_i/k_{T,i}}, \quad k_{T,ang} = \frac{\sum L_i k_{T,i}}{\sum L_i}$$

The thermal conductivity of the active material in the cell in x, y and z direction is defined as below [30]:

$$k_{T,x} = \frac{|y|}{r}\frac{\sum L_i k_{T,i}}{\sum L_i} + \frac{|x|}{r}\frac{\sum L_i}{\sum L_i/k_{T,i}},$$
$$k_{T,y} = \frac{|x|}{r}\frac{\sum L_i k_{T,i}}{\sum L_i} + \frac{|y|}{r}\frac{\sum L_i}{\sum L_i/k_{T,i}}, \quad k_{T,z} = \frac{\sum L_i k_{T,i}}{\sum L_i} \tag{31}$$

The total density of the active material in the cell is expressed in equation below [30]:

$$\rho = \frac{\sum L_i\rho_i}{\sum L_i} \tag{32}$$

The total heat capacity of the active material in the cell is expressed in equation below [30]:

$$C_p = \frac{\sum L_i C_{p,i}}{\sum L_i} \tag{33}$$

2.3. Numerical procedure

The electrochemical and thermal model equations are solved simultaneously using commercial finite-element solver-COMSOL Multiphysics 4.3. The center of the cell is assumed to be fully filled with electrolyte. Five unknowns (ϕ_s, ϕ_l, c_s, c_l, T) are solved using direct solver GMRES subroutine in conjunction with Gauss–Seidal and Multigrid preconditioners with relative convergence tolerance of 10^{-4}. Grid independent test were carried out for all the models. The outputs of the model are temperature, species and

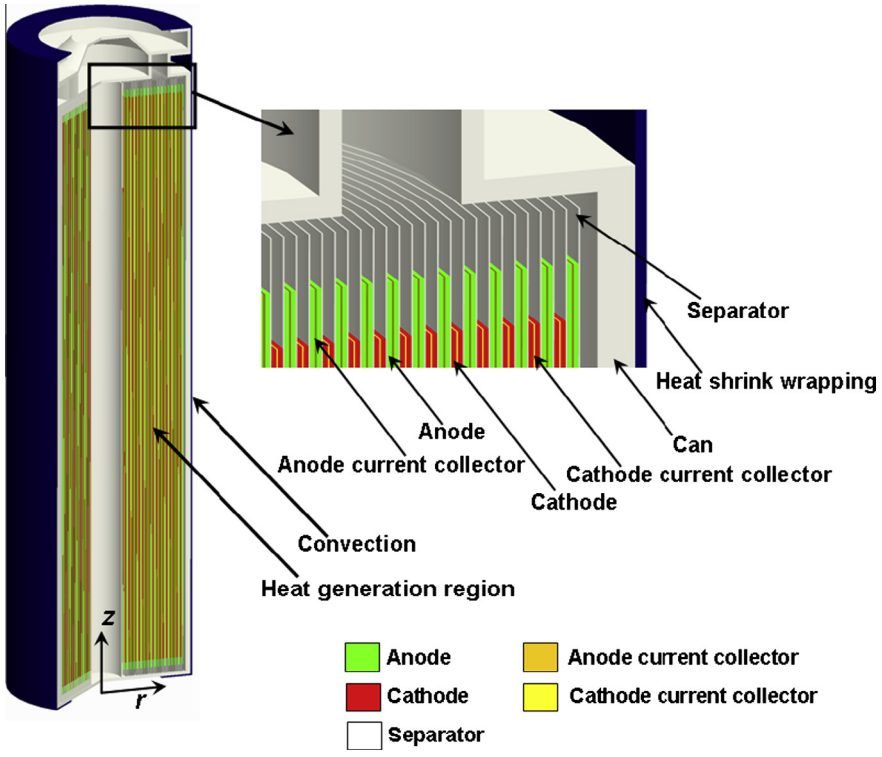

Fig. 4. Schematic of 18650 LFP cell thermal model.

concentration distribution, heat generation and cell potential. Natural convection and radiation are assumed for the heat dissipation of the cell.

3. Experimental

Commercial 1.3 Ah 18650 cells with graphite anode coated on the copper current collector, Lithium Iron Phosphate ($LiFePO_4$) cathode coated on the aluminum current collector, electrolyte ($LIPF_6$) in EC:DEC 1:1 and Polyvinylidene Fluoride (PVDF) separator were used in the experiments. The charging and discharging of the battery were conducted using battery cycler (Maccor Instrument 4000). The simulation model was validated using constant current charge and discharge experiments ranging from $1I_t$ (1.3 A) to $5I_t$ (6.5 A). The I_t-rate as per the standard IEC61434 is defined as [45]

$$I_t = \frac{C}{1\ \mathrm{h}} \tag{34}$$

where I_t represents the discharge current in amperes during 1 h discharge and C is the measured capacity of a battery pack or cell. The cut off voltage for constant current discharging was 2.3 V whereas for constant current charging was 4.2 V and kept at constant voltage until the current dropped to 0.1 A. The surface temperature of the battery was measured using twelve thermocouples (T-types) attached to different locations on the cells. Three thermocouples were attached in the axial direction and on the four sides of the battery surface (Fig. 5). The measurement of battery body temperature during charging and discharging at different I_t-rates were done at room temperature of 25 °C under natural convection. All the tests were repeated three times and the average value was taken. The temperature readings were recorded using the HP 34970A data acquisition system. The effective thermal conductivity of the 20 mm compact $LiFePO_4$ pellet was characterized using C-Therm TCI Thermal Conductivity Analyzer and calculated using Koh and Fortini model as in Eq. (34) because the $LiFePO_4$ powder thermal conductivity cannot be accessed [46].

$$\frac{k_{T,eff}}{k_0} = \frac{1-\xi}{1+11\xi^2} \tag{35}$$

4. Results and discussion

4.1. Evolutions of the cell potential

Fig. 6 shows the capacity of the cell for experiment and numerical simulation at different rates of charging and discharging at constant current. Only the constant current results are shown. The simulation results agreed well with the experimental data with little deviation toward the end of the process. The averaged squared error for the simulated and measured voltage at $1I_t$, $3I_t$, and $5I_t$ charging is 0.0014, 0.00072 and 0.00028 respectively. The averaged squared error of the simulated and measured voltage at $1I_t$, $3I_t$, and $5I_t$ discharging is 0.00018, 0.00043 and 0.00068 respectively. The voltage drop during discharging of the cell was mainly due to the increase of the internal resistance at the end of the discharging process [4]. Solution resistance, contact resistance of the electrode to the current collector, matrix resistance, kinetic resistance and diffusion resistance are the internal resistance of the cell [5]. The steep increase at the end of discharging indicated the positive electrode was fully filled with Li during discharging, the steep increase at the end charging indicated the negative electrode was fully filled with Li. At high I_t-rates, the experimental cell voltage diverged significantly from the simulated open circuit voltage. This was probably due to the difference in the reaction rate, reduction of ohmic resistance and species mass diffusivity change with the temperature [34]. At $5I_t$ of constant current charging, the maximum capacity of the cell was reduced by 20% compared to $1I_t$ (1.12 Ah). On the other hand, the maximum capacity can be drawn from the cell during $5I_t$ of constant current discharging was about 24% less than capacity at $1I_t$ (1.3 Ah). The reduced of the cell capacity at high I_t-rates can be explained by Peukert equation as below [4]:

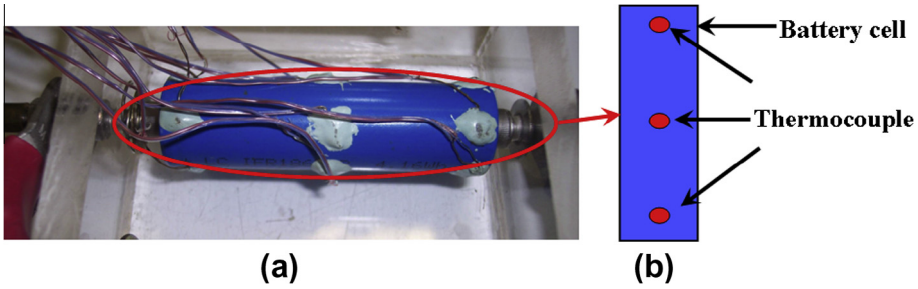

Fig. 5. (a) Experimental setup for temperature measurement. (b) Location of thermocouples attached to the surface of the cell.

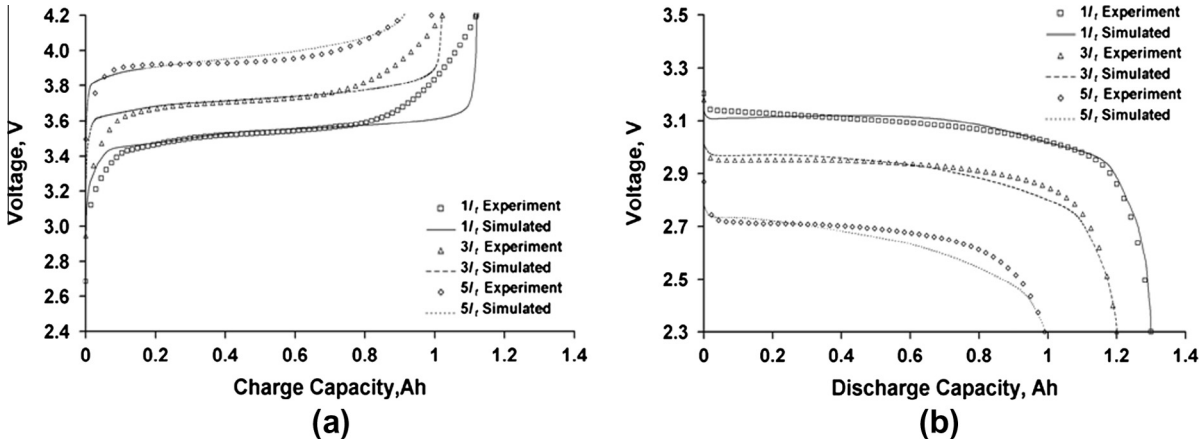

Fig. 6. Experimental and simulation of cell potential for: (a) charging and (b) discharging.

$$C_{bp} = T_{dis} \cdot I_{dis}^{k} \tag{36}$$

Eq. (36) shows that, the higher discharge current and the less capacity available in the in the cell. For charging the cell, there are two modes of operation involved which are constant current and constant voltage to ensure the cell are charged to full capacity.

4.2. Evolutions of the cell temperature

Fig. 7 shows the average measured and simulated temperature rise on the cell surface at different I_t-rates of charging and discharging. Apparently, the average temperatures of the cell were increased stepwise with the state of charge and sharply toward the end of charging or discharging process. This was probably caused by large polarization during the end of charging and discharging process. There was a good agreement between the simulated and measured cell surfaces temperature. As expected, the temperature has a positive correlation with the charging/discharge current. The final temperature changes during charging at $1I_t$, $3I_t$, and $5I_t$ were 3.9 °C, 15.6 °C and 25.2 °C respectively. The averaged squared error for the simulated and measured temperature at $1I_t$, $3I_t$, and $5I_t$ charging is 0.078, 0.050 and 0.055 respectively. The final temperature changes during discharging at $1I_t$, $3I_t$, and $5I_t$ were 6.1 °C, 24.8 °C and 25.1 °C respectively. The averaged squared error of the simulated and measured temperature at $1I_t$, $3I_t$, and $5I_t$ discharging is 0.057, 0.067 and 0.025 respectively. At low I_t-rates of charging or discharging, the heat generated can be dissipated effectively by natural convection and good thermal equilibrium was achieved. Therefore, only small variation of the temperature was observed. As compared to low I_t-rates, large amount of heat

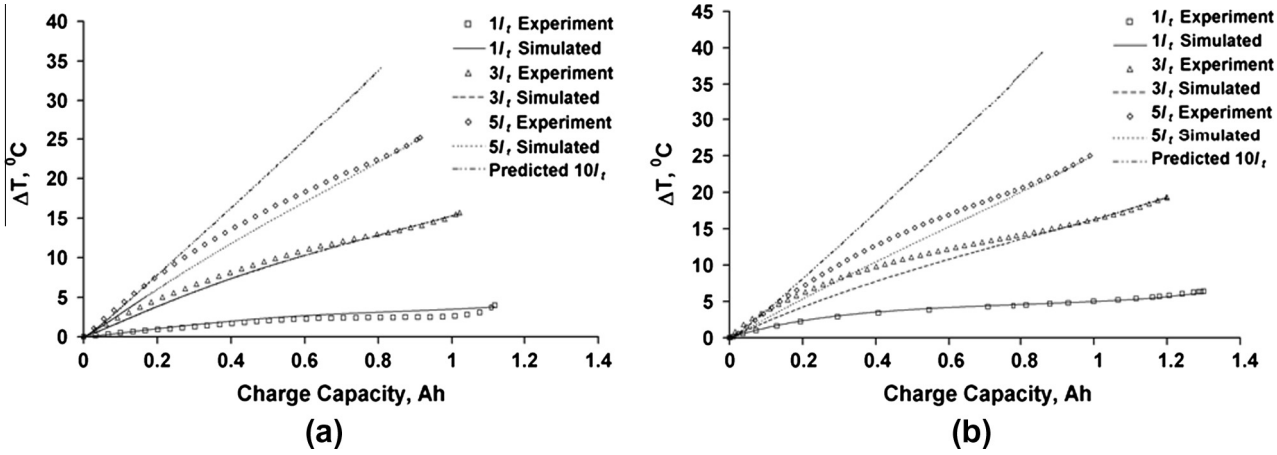

Fig. 7. Experimental and simulated cell temperature: (a) charging and (b) discharging.

was generated at $5I_t$ and the cell did not have sufficient time to dissipate the heat. Hence, the temperature of the cell kept increasing, resulting in reduced ohmic, kinetic and mass transfer losses in the cell and increment in the mass transfer for solid and liquid phases. Average measured surface temperature of the cell deviated significantly with the simulated results during high I_t-rates. This was probably caused by the thermal resistance between the plastic shrink wrap with the battery casing which was not considered in this study. Force convection cooling can be used to suppress the high temperature during high I_t-rates of charging/discharging.

4.3. Heat generation of the cell

Figs. 8 and 9 show the types of heat generation associated with the charging and discharging process. The total heat generations in the cell are comprised of ohmic heat, reaction heat and reversible heat. As the I_t-rates was increased, the cell shifted from its equilibrium state and hence the total heat generation accelerated and this led to rapid increase of the cell temperature as shown in Figs. 8a and 9a. The primary heat generation in the cell was reaction heat. The effect of ohmic and reversible heat became more significant at high I_t-rates. Higher electric conductivity of the graphite and LFP phase resulted lower ohmic heat generation in the matrix phase as shown in Figs. 8b and 9b. Figs. 8c and 9c show that reaction heat was the main source of heat generation during charging and discharging of the cell. Reversible heat was the entropy change in the electrochemical reactions. The reversible heat was an endothermic at the beginning of charging and rapidly became exothermic as the process proceeded and gradually reduced as the charging approached the end as shown in Fig. 8d. During discharging, the reversible heat was gradually changed from endothermic to exothermic and with a bump at the intermediate of the process and reduced sharply towards the end of the process as shown in Fig. 9d. The temperature of the cell grew slower at the initial stage and increased rapidly at the end of discharging which corresponded to the endothermic part of the reversible heat. Therefore, reversible heat was an important parameter for cell modeling. During charging, reaction heat contributed about 80%, ohmic heat contributed about 15% and reversible heat which was the minor source contributed about 5% of the total heat generation. On the other hand, reaction heat contributed about 85%, followed by ohmic heat which was about 10% and reversible heat only contributed about 5% of the total heat generation during discharging.

$10I_t$ of charging was simulated to assess the feasibility of LFP cell for fast charging application. The potential of the cell rose to the cut off voltage of 4.2 V. The final temperature of the cell surface could reach 59 °C as shown in Fig. 7a while the heat generation during the process was illustrated in Fig. 10a. The total heat generation rose nearly 200% compared to $5I_t$. The average heat generation during $10I_t$ discharging was about 40% more than same rate of charging as shown in Fig. 10b with about 40 °C increases in the average cell temperature. However, the optimum operating temperature for Li-ion battery was within 0–40 °C and the battery life cycle, capacity, durability, warranty and safety were highly dependent on the operating temperature. Therefore, pulse charging technique with short relaxation periods and short discharge pulses during charging can be used to substitute conventional direct current charging of the battery to avoid over heating the battery during charging. Besides, active thermal management system must be carefully design for the electric vehicles battery pack using fast charging approach to ensure the cell operate safely, prolong the life span and prevent thermal runaway of the cell.

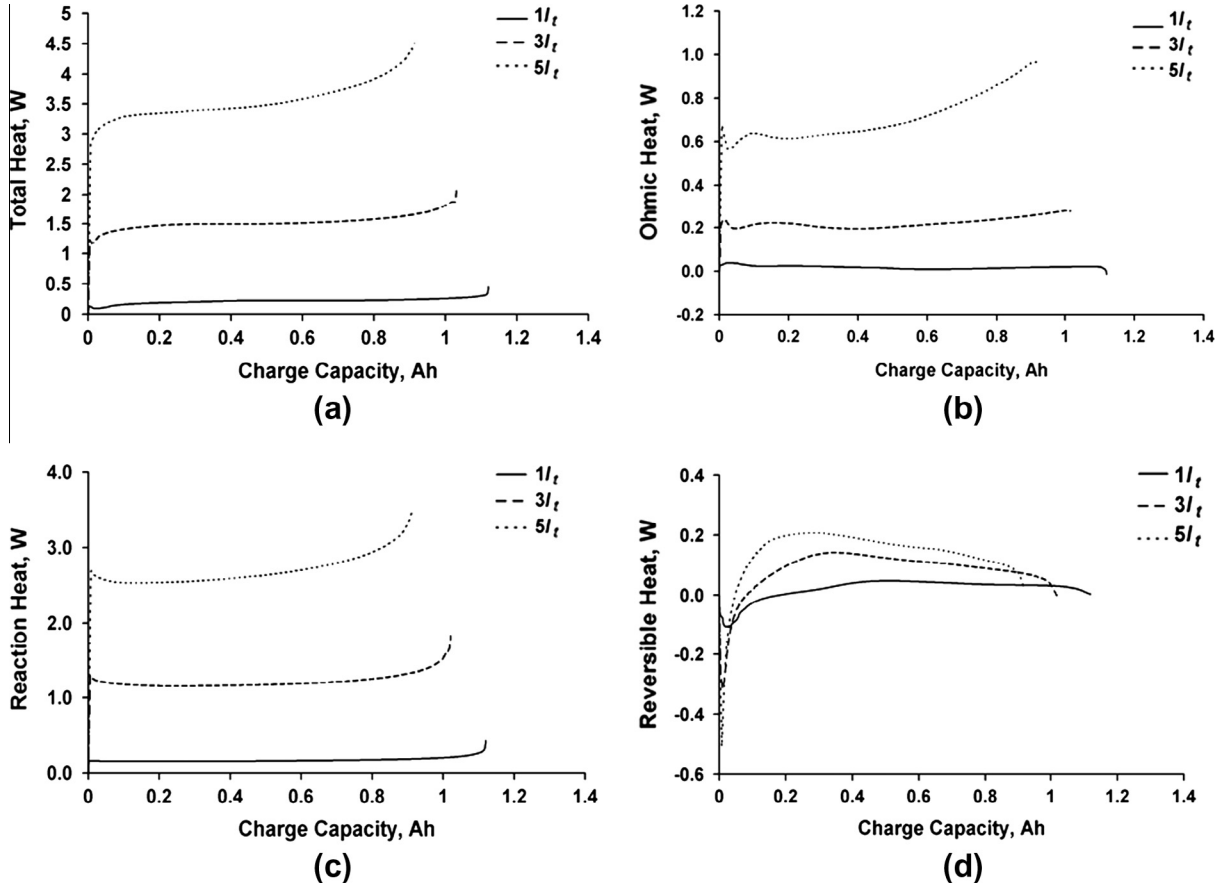

Fig. 8. Heat generation for different I_t-rates of charging: (a) total heat, (b) ohmic heat, (c) reaction heat, and (d) reversible heat.

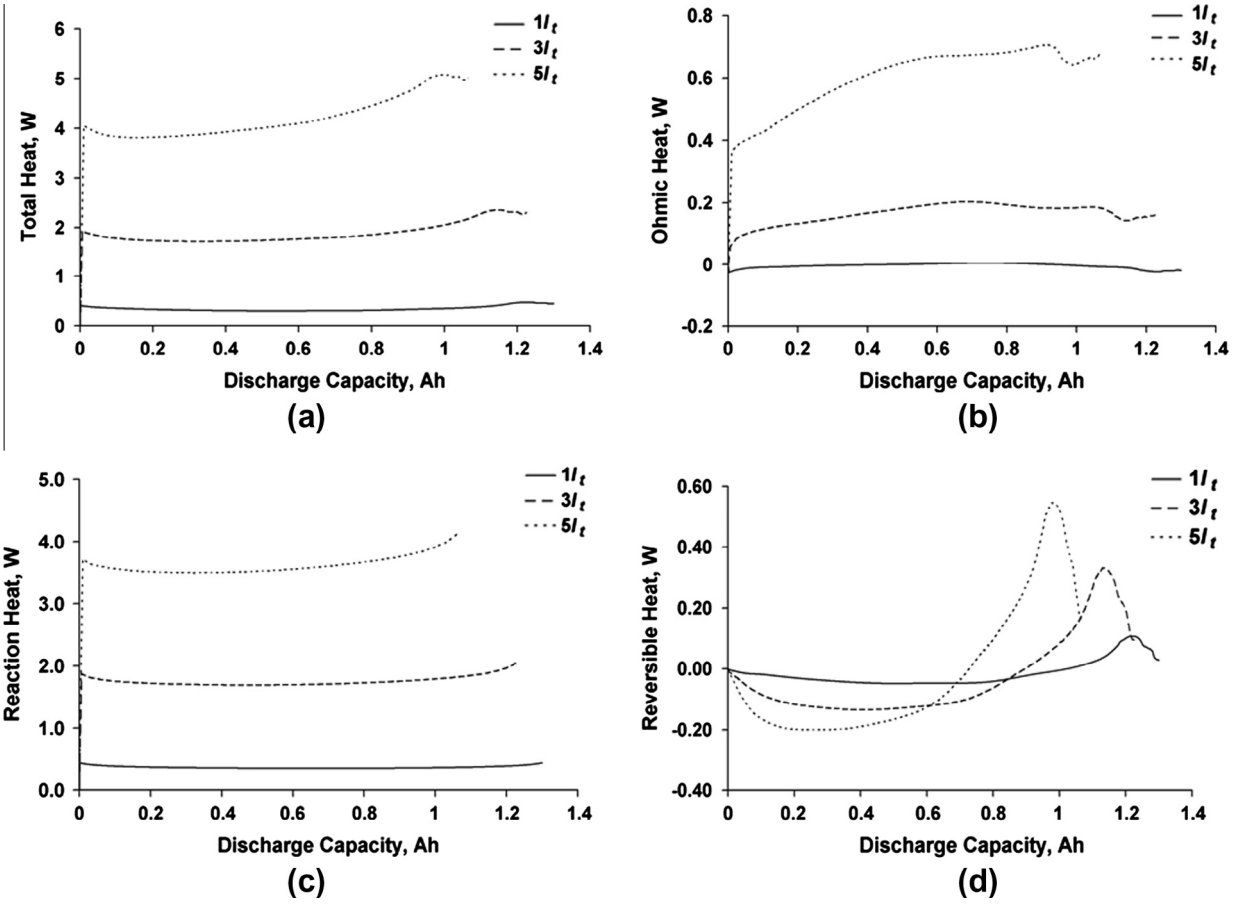

Fig. 9. Heat generation for different I_t-rates of discharging: (a) total heat, (b) ohmic heat, (c) reaction heat, and (d) reversible heat.

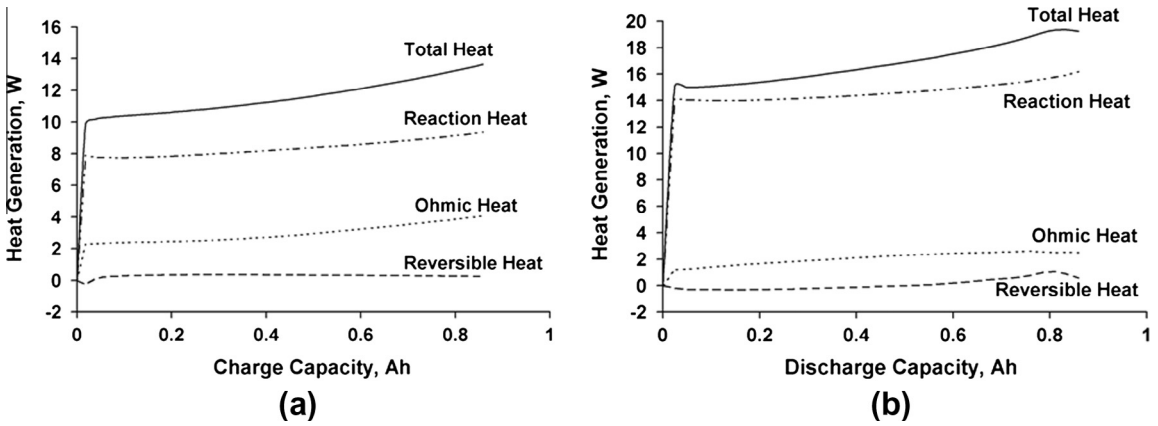

Fig. 10. Heat generation for 10I_t: (a) charging and (b) discharging.

4.4. Concentration distribution of the cell

The concentration profile at the negative electrode, separator and positive electrode for different I_t-rates of charging and discharging are shown in Fig. 11. The performance of the cell was limited by the diffusion of lithium in the electrolyte and active solid material phase. During the charging process, the lithium ion concentration in negative electrode was lower than the positive electrode due to intercalation reaction. The lithium ion distribution was vice versa during the discharging process and mainly determined by the de-intercalation of lithium ion in the negative electrode. The lithium ion concentration gradient increases with the I_t- rates. The lithium ion concentration profile at 1I_t was almost flattened which indicated a better diffusion of the lithium ion in the electrolyte at low I_t-rates. Besides, the Li-ion concentration gradient was the main factor which determined the ohmic heat generation in electrolyte and the ohmic heat generation have a positive correlation with the gradient of the lithium ion concentration.

4.5. Effect of electrical contact resistance

The effect of electrical contact resistance between connectors and cell terminals was also investigated. The contact resistance

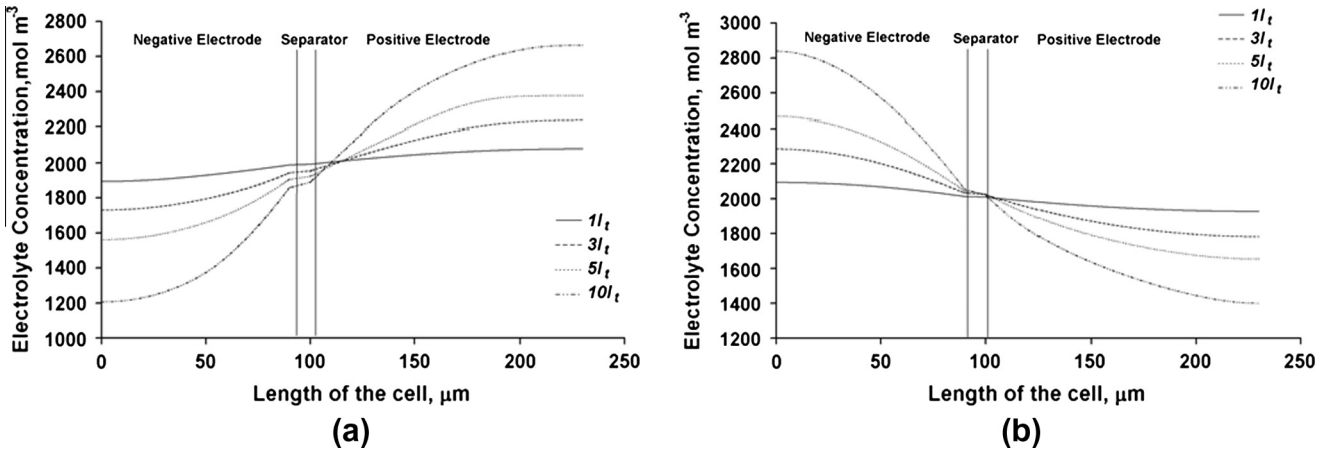

Fig. 11. Concentration profiles of the electrolyte: (a) charging and (b) discharging.

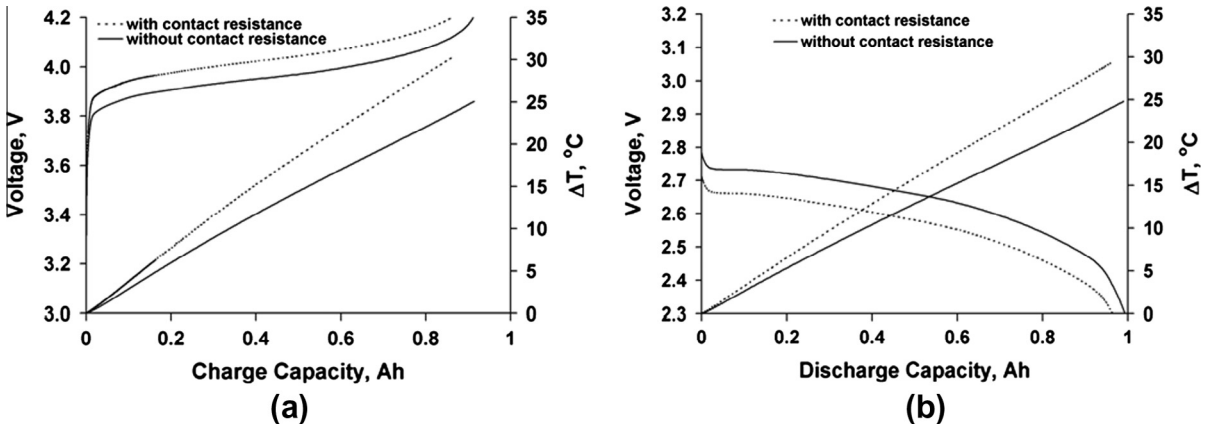

Fig. 12. Effect of contact resistant on cell voltage and average temperature evolutions during $5I_t$: (a) charging and (b) discharging.

was taken as 10 mΩ based on worst case scenario [38]. These external energy losses have always been overlooked in the energy management of the battery pack. The electrical power loss due to electrical contact resistance was defined as $P = I^2(R_{cc}/A_{cc})$. This electrical power loss was in the form of heat generated at the connector-cell terminal interface. The higher I_t-rates resulted in higher heat generation rate occurred at $5I_t$. Fig. 12 shows the effect of the electrical contact resistance on the cell potential and temperature evolutions during $5I_t$ of charging and discharging. The power loss was about 0.42 W at each terminal of the cell. Compared to the charging process without contact resistance, the average temperature rise of the cell during charging with contact resistance was increased from 25.2 °C to 30.4 °C. The capacity of the cell was reduced by 5.4% to overcome the power loss caused by the electrical contact resistance. During the discharging process, the electrical contact resistance reduced the maximum capacity of the cell at constant current discharging by 3%. The average temperature rise of the cell during the end of discharge was increased from 24.8 °C to 29.4 °C. The effect of the contact resistance on the heat generation during charging and discharging at $5I_t$ is shown in Fig. 13. As shown in Fig. 13, total heat transfer during $5I_t$ charging and discharging

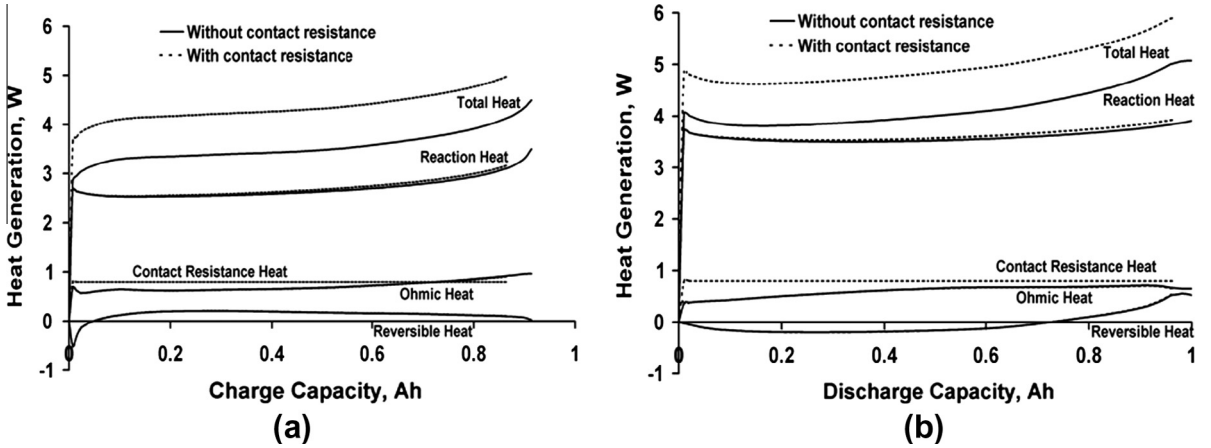

Fig. 13. Heat generation for $5I_t$ with and without effect of contact resistance: (a) charging and (b) discharging.

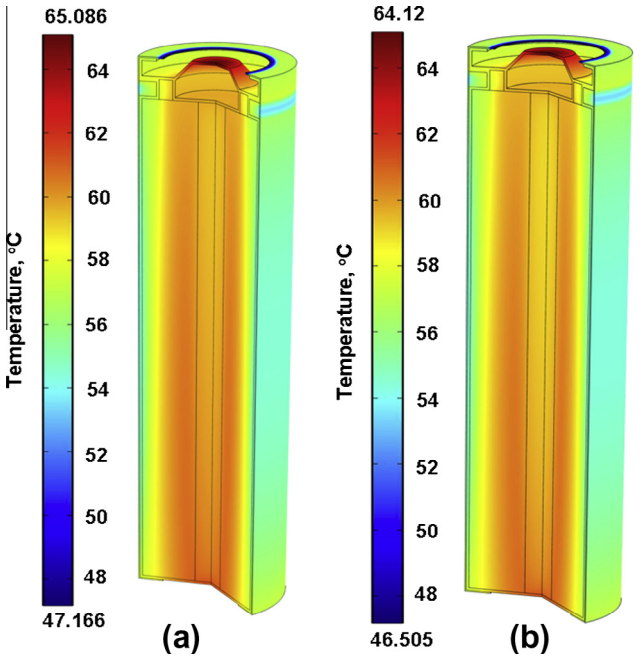

Fig. 14. Contour of temperature distribution in the cell during $5I_t$ of: (a) charging and (b) discharging.

for the cell with poor contact resistance is higher than the cell without consideration of the effect of contact resistance. Average rise in total heat generation for cell during $5I_t$ charging or discharging with poor contact resistance is about 20% and mainly contributed by contact resistance heat. The effect of electric contact resistance is localize and concentrated at the terminals and further deteriorate the temperature uniformity of the cell. Fig. 14 shows the contours plot of the cell temperature distribution at the end of charging and discharging. There were hot spots at the top and bottom end of the cell. Large temperature gradient was found across the cell in radial direction. The temperature distribution in axial direction was uniform due to large thermal conductivity in this direction. So the main temperature variation was in radial direction, irrespective of both axial and angular direction. The temperature variation across the radial direction was about 10 °C during end of the charging/discharging. The cell temperature was at the higher limit of the allowable temperature variation within the cell. The contact resistance effect decreased the temperature uniformity within the cell dramatically and further induced a performance decline due to unbalanced charging and discharging. Hence, this is a significant factor which should be accounted for the cells connector design and battery assembly. Therefore, rigid contact between the connectors and terminals is needed to reduce the power losses and improve the nonuniformity of the temperature.

5. Conclusions

An electrochemical coupled with thermal model was applied to investigate the electrochemical and thermal behavior of the cell during charging and discharging process. Good agreement between the simulation results and experiment was achieved. The heat generated in the cell was contributed by reaction heat, ohmic heat and reversible heat. Numerical simulation results showed that reaction heat was the major heat source during the charging and discharging process. The heat generation rate of the cell was positively correlated with the I_t-rates. In addition, imperfect contact between the terminals of the cell will caused development of large temperature gradients within the cell, affecting the cell capacity. The difference between maximum and minimum temperatures at the end of the charging/discharging process was about 10 °C, which was at the high side of the allowable temperature variation of Li-ion battery. Therefore, a proper cooling system design and assembly of the battery and connectors is needed for the EV and HEVs using fast charging approach.

References

[1] Nagaura T. A lithium ion battery. In: 4th International rechargeable battery seminar, Dearfield Beach, Florida, 1992..
[2] Dhameja S. Electric vehicle battery systems. USA: Newnes; 2002.
[3] Zhang SS. An overview of the development of Li-ion batteries: From material, single cell to battery pack, in advanced materials and methods for Lithium-ion batteries. Canada: Research Signpost; 2007. p. 1–22.
[4] Omar N, Daowd M, Van Den Bossche P, Hegazy O, Smekens J, Coosemans Th, et al. Rechargeable energy storage systems for plug-in hybrid electric vehicles-assessment of electrical characteristics. J Energies 2012;5:2952–88.
[5] Srinivasan V, Newman J. Discharge model for the lithium iron-phosphate electrode. J Electrochem Soc 2004;151:A1517–29.
[6] Schalkwijk WA, Scrosati B. Advances in Lithium-ion batteries. New York, USA: Kluwer Academic/Plenum Publisher; 2002.
[7] He H, Xiong R, Guo H, Li S. Comparison study on the battery models used for energy management of batteries in electric vehicles. Energy Convers Manage 2012;64:113–21.
[8] Tsang KM, Sun L, Chan WL. Identification and modeling of Lithium ion battery. Energy Convers Manage 2010;51:2857–62.
[9] Smith KA, Rahn CD, Wang CY. Control oriented 1D electrochemical model of lithium ion battery. Energy Convers Manage 2007;48:2565–78.
[10] Kumaresan K, Sikha G, White RE. Thermal model for a Li-ion cell. J Electrochem Soc 2008;155:A164–71.
[11] Kim GH, Pesaran A, Spotnitz R. A three-dimensional thermal abuse model for lithium-ion cells. J Power Source 2007;170:476–89.
[12] Sato N. Thermal behavior analysis of lithium-ion batteries for electric and hybrid vehicles. J Power Source 2001;99:70–7.
[13] Jeon DH, Baek SM. Thermal modeling of cylindrical lithium ion battery during discharge cycle. Energy Convers Manage 2011;52:2973–81.
[14] Somasundaram K, Birgersson E, Mujumdar AS. Thermal-electrochemical model for passive thermal management of a spiral-wound lithium-ion battery. J Power Source 2012;203:84–96.
[15] Chen Y, Evans JW. Thermal analysis of Lithium-Ion batteries. J Electrochem Soc 1996;143:2708–12.
[16] Cai L, White RE. Mathematical modeling of a lithium ion battery with thermal effects in COMSOL Inc. Multiphysics (MP) software. J Power Source 2011;196:5985–9.
[17] Guo M, Sikha G, White RE. Single-particle model for a lithium-ion cell: thermal behavior. J Electrochem Soc 2011;158:A122–32.
[18] Gu WB, Wang CY. Thermal and electrochemical coupled modeling of a lithium-ion cell. In: 196th meeting of the Electrochemical Society, Honolulu, USA, 2000, p. 748–62.
[19] Bandhauer TM, Garimella S, Fuller TF. A critical review of thermal issues in Lithium-ion batteries. J Electrochem Soc 2011;158:R1–R25.
[20] Ramadesigan V, Northrop PWC, De S, Santhanagopalan S, Braatz RD, Subramanian VR. Modeling and simulation of lithium-ion batteries from a systems engineering perspective. J Electrochem Soc 2012;159:R31–45.
[21] Forgez C, Do DV, Friedrich G, Morcrette M, Delacourt C. Thermal modeling of a cylindrical $LiFePO_4$/graphite lithium-ion battery. J Power Source 2010;195:2961–8.
[22] Kim US, Shin CB, Kim CS. Modeling for the scale up of a lithium ion polymer battery. J Power Source 2009;189:841–6.
[23] Inui Y, Kobayashi Y, Watanabe Y, Watase Y, Kitamura Y. Simulation of temperature distribution in cylindrical and prismatic lithium ion secondary batteries. Energy Convers Manage 2007;48:2103–9.
[24] Al Sakka M, Gualous H, van Mierlo J, Culcu H. Thermal modeling and heat management of supercapacitor modules for vehicle applications. J Power Sour 2009;194:581–7.
[25] Doyle M, Newman J. Comparison of modeling predictions with experimental data from plastic lithium ion cells. J Electrochem Soc 1996;143:1890–903.
[26] Yamada A, Kudo Y, Liu KY. Phase diagram of $Li_x(Mn_yFe_{1-y})PO_4 (0 < x,\ y < 1)$ batteries and energy conversion. J Electrochem Soc 2001;148:A1153–8.
[27] Thorat IV, Joshi T, Zaghib K, Harb JN, Wheeler DR. Understanding rate-limiting mechanisms in $LiFePO_4$ cathodes for Li-ion batteries. J Electrochem Soc 2011;158:A1185–93.
[28] Taheri P, Hsieh S, Bahrami M. Investigating electrical contact resistance losses in lithium-ion battery assemblies for hybrid and electric vehicles. J Power Source 2011;196:6525–33.
[29] Pesaran A, Bharathan D, Kim GH. Improving battery design with electro-thermal modeling. In: IEEE 2005 vehicle power and propulsion conference, Illinois, USA, 2005, p. 368–75.
[30] Chen SC, Wang YY, Wan CC. Thermal analysis of spirally wound lithium batteries. J Electrochem Soc 2006;153:A637–648.

[31] Srinivasan V. BATT November 2010 quarterly report. Berkeley: Berkeley National Laboratory; 2010.
[32] Wang CS, Kasavajjula US, Arce PE. A discharge model for phase transformation electrodes: formulation, experimental validation and analysis. J Phys Chem C 2007;111:16656–63.
[33] Smith K, Wang CY. Power and thermal characterization of a lithium-ion battery pack for hybrid electric vehicles. J Power Source 2006;160:662–73.
[34] Srinivasan V, Wang CY. Analysis of electrochemical and thermal behavior of Li-ion cells. J Electrochem Soc 2003;150:A98–106.
[35] Fang W, Kwon OJ, Wang CY. Electrochemical thermal modeling of automotive Li-ion batteries and experimental validation using a three electrode cell. Int J Energy Res 2010;34:107–15.
[36] Thorat IV. Understanding performance limiting mechanisms in Li-ion batteries for high rate applications. Thesis (PhD). USA: Brigham Young University; 2009.
[37] Mikron, Table of emissivity of various surfaces. <http://www.eng.lbl.gov/~dw/projects/DW4229_LHC_detector_analysis/calculations/emissivity2.pdf> [Retrieved August 2012].
[38] Fu R, Choe SY, Jackson RL, Flowers GT, Bozack MJ, Liang Zhong, et al. Vibration-Induced changes in the contact resistance of high power electrical connectors for hybrid vehicles. IEEE Trans Comp Pack Manual Tech 2012;2:185–93.
[39] Safari M, Delacourt C. Modeling of a commercial graphite/$LiFePO_4$ cell. J Electrochem Soc 2011;158:A562–71.
[40] Kumaresan K, Sikha G, White RE. Thermal model for a Li-ion cell. J Electrochem Soc 2008;155:A164–171.
[41] Viswanathan VV, Choi D, Wang D, Xu W, Towne S, Williford RE, et al. Effect of entropy change of lithium intercalation in cathodes and anodes on Li-ion battery thermal management. J Power Sour 2010;195:3720–9.
[42] Menard L, Fontes G, Astier S. Dynamic energy model of a lithium-ion battery. Math Comp Sim 2010;81:327–39.
[43] van Schalkwijk A, Scrosati B. Advances in Lithium-ion batteries. New York: Kluwer Academic; 2002.
[44] Rao L, Newman J. Heat generation rate and general energy balance for insertion battery systems. J Electrochem Soc 1997;144:2697–704.
[45] Omar N, Daowd M, Hegazy O, Mulder G, Timmermans J, Coosemans Th, et al. Standardization work for BEV and HEV applications: critical appraisal of recent traction battery documents. J Energies 2012;5:138–56.
[46] Koh JCY, Fortini A. Prediction of thermal conductivity electrical resistivity of porous metallic materials. Int J Heat Mass Trans 1973;16:2013–22.